Design, Analysis and Simulation for Development of the First Clinical Micro-CT Scanner[1]

Ge Wang, PhD, Shiying Zhao, PhD, Hengyong Yu, PhD, Charles A. Miller, PhD, Paul J. Abbas, PhD, Bruce J. Gantz, MD, Seung Wook Lee, PhD, Jay T. Rubinstein, PhD, MD

In this article, we propose to develop the first clinical micro-CT (CMCT) system for human temporal bone imaging in vivo. This CMCT system consists of medical CT and micro-CT scanners either as separate components or in a combination, a cross-modality registration mechanism such as a facial surface scanner, and associated software. This system integrates the strengths of state-of-the-art medical CT and micro-CT techniques to achieve a spatial resolution that is much higher than currently available for inner ear imaging at acceptable dose levels. Our design, analysis, and simulation results demonstrate that the CMCT system is feasible for inner ear imaging and other clinical applications. For example, the CMCT system has the potential to improve the safety of guiding cochlear implant electrodes within the inner ear and assist the placement of inner ear microcatheters for delivery of gene modification therapy or administration of neurotrophic factors. Imaging of microarchitectures of the cancellous bone would be also an important application.

Key Words. Computed tomography (CT); micro-CT; local tomography; temporal bone imaging.

During the past 30 years, medical X-ray CT scanners have continued to evolve toward increasingly refined image quality while maintaining or reducing the X-ray dose to the patient. Currently, state-of-the-art medical CT scanners allow about a 0.3-mm in-plane resolution and a 0.5-mm through-plane resolution, which comes close to the resolution needed to visualize individual electrodes of the cochlear implant in a CT scan of the head. However, there are important and immediate clinical needs for dramatically better image resolution. Particularly, with a 3- to 5-fold higher image resolution, we would be able to map the cochlear structures significantly better, which could be invaluable for electrophysiological modeling, inner ear implant design, cochlear implant programming, as well as diagnosis and monitoring of various inner ear diseases.

In parallel to the development of medical CT scanners, micro-CT devices have recently become popular for small animal studies. Although there has been a rapid refinement in the micro-CT technology, much effort has been limited to small fields of view, matching the sizes of small animals. Most of the existing micro-CT systems employ CCD cameras, microfocus x-ray tubes, and have image resolutions between 10–50 μm. However, these imaging systems do not permit imaging of the patient. There has been an increasing interest in development of the microimaging capability for patient studies. The SCANCO Company now markets a scanner with a less than 100 μm voxel size for use in the ankle and wrist. DiBianca et al. developed a variable resolution x-ray (VRX) detection method for increasing the resolution of a "clinical" CT scanner by means of tilting the detector array at an angle to the X-ray beam

Acad Radiol 2005; 12:511–525

[1] From the CT/Micro-CT Laboratory, Department of Radiology, University of Iowa, Iowa City, IA 52242 (G.W.,S.Z.,H.Y.); Department of Otolaryngology, University of Iowa, Iowa City, IA (C.A.M., B.J.G.); Department of Speech Pathology & Audiology, University of Iowa, Iowa City, IA (P.J.A.); Virginia Merrill Bloedel Hearing Research Center, University of Washington, Seattle, WA (J.R.). Neutron Imaging Lab, HANARO Center, Korea Atomic Energy Research Institute, Daejeon, South Korea. Received October 29, 2004; revision requested November 22; revision received and accepted January 3, 2005. **Address correspondence to** G.W. e-mail: ge-wang@uiowa.edu

doi:10.1016/j.acra.2004.01.024

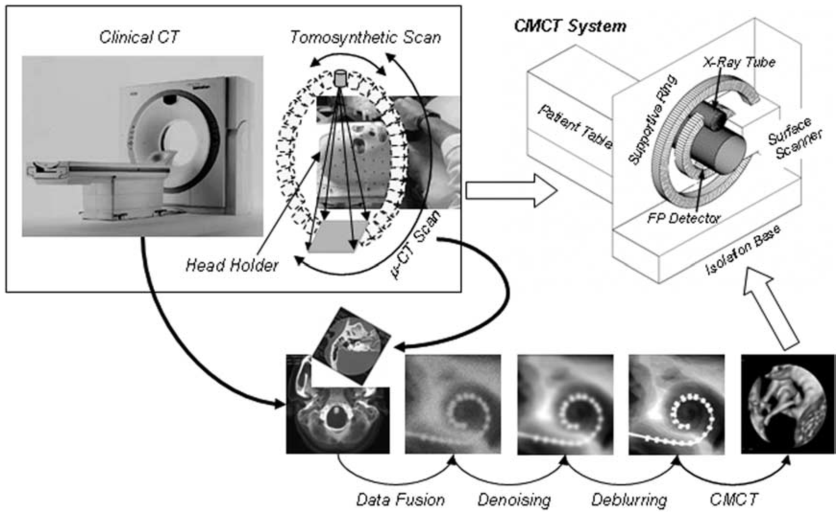

Figure 1. Overview of the project development of clinical micro-CT for temporal bone imaging.

(1,2). This approach integrates high-resolution data into 'low'-resolution scan data.

Since 2003, we have been working to develop a clinical micro-CT (CMCT) system, the first of its kind initially targeting the human temporal bone imaging in vivo (3). This system will integrate the strengths of state-of-the-art medical CT and micro-CT techniques to achieve a spatial resolution that is much better than that currently available. An enabling technology for CMCT without increasing patient dose is local CT reconstruction of a volume of interest (VOI). This solution is especially suitable for imaging the inner ear because of its small volume, bony structures, thin features, and stationary nature. Although several methods have been proposed for local CT, such as lambda-tomography (4,5) and wavelet multi-resolution local tomography (6–10), few of them have ever been really applied in clinical arenas, due to reconstruction artifacts and/or hardware obstacles. Other inner ear scanning methods based on micro-CT and MR were also developed (11,12), which attracted great interest and illustrate that our proposed CMCT technology is a further step in the right direction of imaging microscopic structures in humans.

In the following, the feasibility of our CMCT concept is demonstrated. Our design goal is to realize micro-CT resolution in the framework of medical CT imaging without significantly increasing radiation dose. Despite other important applications, our initial clinical motivation is for imaging of the temporal bone with an emphasis on the cochlea. In sections I and II, we describe the basic architecture and the design principles of the CMCT system, analyze the involved dose levels, and propose an image reconstruction strategy. In Section III, we present preliminary CMCT reconstructions from numerically simulated and real CT/micro-CT data. In Section IV, we discuss relevant issues and conclude the article.

SYSTEM DESIGN

System description

As shown in Figure 1, the proposed CMCT system consists of medical CT and micro-CT scanners either as separate components or in combination, a cross-modality registration system such as a facial surface scanner (a device for capture of 3D surface information using optical means), and associated software. The micro-CT component includes a small focal spot X-ray tube, a high-resolution detector, an optical facial surface scanner as an example of a cross-modality registration system, a patient table/bench, and possibly a vibration isolation base for micro-CT. During a patient exam, a standard medical CT protocol is first executed as routinely done in the clinical practice. Then, the facial surface scan is performed after the patient is positioned for a local micro-CT scan. The facial surface models are built from the medical CT scan and the optical facial surface scan, respectively. Finally, the patient position or the microimaging chain is adjusted according to the surface models so that the center of a prescribed VOI coincides with the isocenter of the gantry, or with respect to other landmarks in the VOI.

The CMCT software components include 2 surface modeling modules dealing with the CT image volume and optical data respectively, data/image registration programs, a local micro-CT reconstruction/microtomosynthesis engine, and a number of image-processing utilities. While the global low-resolution projection data are from the medical X-ray CT scan, the local high-resolution projection data are acquired in the same patient during a local micro-CT scan. Finally, a volumetric CMCT image of the VOI can be reconstructed by integrating the global and local projection data and applying a modified Feldkamp algorithm (13) or another suitable reconstruction method.

Design Principles

In the state-of-the-art multi-slice spiral CT scanner, the sizes of the focal spot and detector cell are typically millimeter- or submillimeter-sized with subsecond rotation time and sub-mm image resolution. We have estimated that for the proposed CMCT to achieve an image resolution of 60–100 μm, which is 3–5 times better than that of the medical CT scanner, we need to scale the focus spot and detector cell sizes to 0.1–0.2 mm. If such a micro-CT scan had to be performed globally, it would take a long time and imply a high patient dose. However, our CMCT is only needed to reconstruct a small VOI containing the inner ear, especially the cochlea, with the desired micro-CT image resolution. For an optimized design of our proposed CMCT system, we will utilize the following strategies:

1. Adapt a state-of-the-art data acquisition system (DAS) with high quantum efficiency and low dark current;
2. Limit an X-ray scan region to a small VOI using various data/image registration and navigation schemes;
3. Apply super-short-scan techniques (14,15) for reconstruction of the VOI;
4. Develop source deblurring algorithms to allow relatively large focal spot sizes (for example, ~0.5 mm in diameter);
5. Develop wavelet-denoising techniques to suppress image noise.

Dose Analysis

Total dose analysis.—The signal-to-noise ratio (SNR) refers to the magnitude of the signal compared to the magnitude of the random fluctuations in each image pixel. Mathematically, it is defined as the ratio between the measured signal strength and image noise standard deviation. An adequate SNR is a key requirement for image reconstruction. Image noise arises from various sources in the CT and micro-CT data acquisition systems (DAS). The 3 primary factors contributing to data noise are *photon noise*, *dark noise*, and *read noise*, which are described as follows.

Photon noise originates from the detectors, which convert incoming photons into photoelectrons. These photoelectrons carry not only the signal but also statistical variation in the photon number received by a detector. It is well known that the number of photoelectrons follows a Poisson distribution, yielding a square root relationship for SNR. *Dark noise* is due to thermally generated electrons within the detector architecture. Dark current is nothing but the rate of thermal electrons, which is temperature dependent. Like the number of photoelectrons, the number of thermal electrons obeys a Poisson distribution. *Read noise* happens in the DAS circuitry. The on-chip preamplifier produces a primary part of read noise. Spurious charge also makes a significant contribution. Overall, the SNR of a DAS can be expressed as

$$SNR = \frac{Q_e \Phi t}{\sqrt{Q_e\,(\Phi + B)t + Dt + N_r^2}}, \qquad (1)$$

where Φ denotes the incident photon flux, B the background photon flux, Q_e the detective quantum efficiency (DQE), D the dark current, N_r the read noise, and t the exposure time. When the number of photons is sufficiently small, read noise exceeds photon noise. This state is referred to as "*read-noise limited.*" We can similarly define the most common case, which is "*photon-noise limited.*"

To achieve the desired image resolution with the proposed CMCT, it is necessary to reduce the focal spot diameter of the X-ray tube and the detector cell dimensions. If an X-ray spot size and the detector pixel size are reduced by linear factors m and n, respectively, then both the incident photon flux and the photon number upon each detector, which are respectively proportional to the spot area and detector area, are reduced by m^2 and n^2

Table 1
Estimated Relative Scan Time and Radiation Dose (in Relative Units) for the Proposed CMCT System*

	m									
	2		3		4		5		10	
n	Time	Dose	Time	Dose	Time	Dose	Time	Dose	Time	Dose
2	32	0.08	108	0.12	256	0.16	500	0.20	4000	0.40
3	72	0.18	243	0.27	576	0.36	1125	0.45	9000	1.60
4	128	0.32	432	0.48	1024	0.64	2000	0.80	16000	3.60
5	200	0.50	675	0.75	1600	1.00	3125	1.25	25000	6.40
10	800	2.00	2700	3.00	6400	4.00	12500	5.00	100000	10.00

*m and n denote the linear factors by which an x-ray spot size and the detector pixel size are respectively reduced.

times. According to Eq. (1), the SNR with this refined configuration would become

$$SNR_{m,n} \approx \frac{Q_e \Phi t}{\sqrt{Q_e(\Phi + B)t + m^2n^2Dt + m^2n^2N_r^2}} \frac{1}{mn}. \tag{2}$$

Consequently, for the same SNR as that with medical CT the dark current and read noise must be reduced, and the scan duration must be prolonged for each projection. If we assume for simplicity's sake that the number of views is inversely proportional to the spot size, then the total scan time should be prolonged by up to m^3n^2 times.

To estimate the effective dose resulting from the changes in the source and detector parameters, we need the source factor $1/m^2$, the prolongation factor m^3n^2, and the VOI factor a/A, where A and a are respectively the average projection areas of the global head region and a VOI in the region. The fraction of the total dose involved with CMCT relative to the standard dose of the head CT becomes

$$\frac{DOSE_{m,n}}{DOSE} \propto mn^2 \frac{a}{A}, \tag{3}$$

where $DOSE$ is the effective dose with the medical head CT. If we use a ratio $a/A \approx 0.01$, the relative scan time and radiation dose are listed in Table 1. For $m = 3$ and $n = 4$, the integrated dose would be just about 1/2 of the normal head CT dose, and the total scan time of CMCT would be about 10 minutes (note that the roles for m and n are not interchangeable because we have assumed that the number of views is inversely proportional to the spot size).

Organ dose analysis.—To estimate the radiation dose for the proposed CMCT system, we use the theoretical formulas derived for a uniform cylindrical phantom (16,17). The dose, $DOSE$, at the center of the phantom of radius R can be expressed in terms of the photon flux Φ as follows:

$$DOSE = \frac{\Phi e^{-\mu R} E \mu_{en}}{\rho}, \tag{4}$$

where E is the energy of primary photons, μ the attenuation coefficient, μ_{en} the energy absorption coefficient, and ρ the mass density. The total number of photons N_{det} to the detector cell of width δ and height Δz is then given by

$$N_{det} = Q_e \Phi e^{-2\mu R} \Delta z \delta = \frac{e^{-\mu R} \Delta z \delta Q_e (DOSE)}{(\mu_{en}/\rho)E}. \tag{5}$$

The QDE Q_e of the detector can be computed based on the following equation:

$$Q_e = 1 - e^{-\mu_{ph} t_{ph}}, \tag{6}$$

integrated over the energy spectrum of the X-ray tube, where t_{ph} is the thickness of the phosphor screen, and μ_{ph} is the attenuation coefficient.

The variance, σ^2, in a reconstructed image is inversely proportional to N_{det} and the transaxial area of a voxel δ^2:

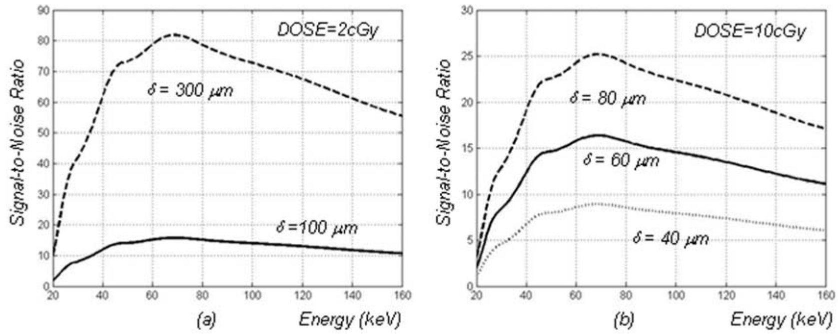

Figure 2. Plots for signal-to-noise ratio versus photon energy for fixed organ dose and spatial resolution **(a)** the limiting performance of the current clinical CT (δ = 300 μm) versus the lower bound performance of the proposed CMCT (δ = 100 μm), and **(b)** the target best performance of the CMCT (δ= 80 μm) and a more aggressive performance (δ = 40–60 μm) at the same organ dose.

$$\sigma^2 = \frac{K}{N_{\text{det}}\delta^2}. \tag{7}$$

Therefore, the square of the SNR is given by

$$\text{SNR}^2 = \frac{\mu^2}{\sigma^2} = \frac{N_{\text{det}}\mu^2\delta^2}{K} = \frac{\delta^3 \Delta z \mu^2 Q_e(DOSE)}{KE(\mu_{\text{en}}/\rho)e^{\mu R}}. \tag{8}$$

The factor K is related to the filtration step of the reconstruction process, reflects the effects of the ramp and apodization filters employed in filtered backprojection, and can be computed as follows (18):

$$K = \delta^3\pi^2\int_{-\Delta t/2}^{\Delta t/2} f^2 \left| W(f) \right|^2 df, \tag{9}$$

where f denotes the spatial frequency, Δt is the detector pixel size projected to the isocenter which can be set to δ, and $W(f)$ the apodization window function. Specifically, for the Hamming window

$$W(f) = 0.54 + 0.46 \cos(2\pi f \Delta t), \tag{10}$$

$K = 0.091$ (19). In terms of units keV for energy, cm for length, gram for weight, and cGy for dose, the SNR formula becomes

$$\text{SNR} = 249830.0953\sqrt{\frac{\delta^3 \Delta z \mu^2 Q_e(DOSE)}{KE(\mu_{\text{en}}/\rho)e^{\mu R}}}. \tag{11}$$

The above relationship allows the plotting of SNR versus dose at the center of the phantom, which is a good indication of the potential detriment to the patient. For the uniform phantom of 80% water and 20% bone, Figure 2 shows the SNR as a function of the tube voltage for a current medical CT and the proposed CMCT scanners at relevant dose levels, where the detector QDE $\eta = 0.8$ and slice-thickness $\Delta z = 0.75$ mm. As shown in Figure 2(a), there is a ~5-fold drop in SNR when the CMCT resolution is 100 μm at the dose level 2cGy, which is a 3-fold improvement of the clinical CT limiting resolution. However, the compromised SNR is still over 10, which is quite sufficient for diagnosis based on our experience. If even higher resolution is needed, such as 60 μm, the dose should be increased to 10 cGy according to Figure 2(b).

In reference to Figure 2, several comments are in order on the effective organ dose. Now, the target resolution of the CMCT system is set to 60–100 μm, equivalent to a 3- to 5-fold improvement relative to the limiting resolution of a state-of-the-art medical CT scanner. Given the effective dose of ~3.5 cGy for a head CT scan using our Siemens SOMATOM Sensation 16 scanners (Erlangen, Germany), if the spatial resolution is improved by a factor of 3–5 in the entire field of view with other image quality indexes fixed, the radiation dose would be increased by a factor between 27 and 125. However, the current CT image noise is only ~60 HU using a standard temporal bone imaging protocol (20). Doubled or tripled noise levels are still much less than the contrast between bone and tissue (>1,000 HU), and should be tolerable for bony structure imaging. In this way, the dose can be greatly reduced to be less than the critical threshold for acute radiation syndromes to begin. Also, more dose-reduction means are available, including local region scanning, statistical reconstruction, source deblurring, wavelet denoising, and so on. Briefly speaking, in the local region–based scanning, the X-ray source only radiates at most 1/10 of the transverse field of view, which reduces the total dose by an order of magnitude (~1/10). The statistical reconstruction would maximize the likelihood subject to prior knowledge and should reduce the organ dose by about half (~1/2) (21). The source deblurring techniques may improve image resolution significantly without increasing image noise (20). A well-designed wavelet denoising method may reduce image noise effectively without compromising image resolution. Additionally, if the tomosynthesis mode is used, the dose can be reduced by another order of magnitude. Therefore, our conservative estimation is that the proposed CMCT system would only need a dose comparable to that of the clinical CT head scan to improve image resolution in a local region of interest by 3–5 times. This 3- to 5-fold improvement relative to the clinical CT performance would be sufficient for our applications.

IMAGE RECONSTRUCTION

VOI Reconstruction

It is well known that the local CT problem is not uniquely solvable (22). The reconstruction of a 2D region-of-interest (ROI) from local projection data suffers from image cupping and intensity shifting artifacts. Since Feldkamp-type algorithms for cone-beam CT perform weighted 2D fan-beam reconstructions from data associated with tilted fans, the Feldkamp-type reconstruction of a VOI from local projection data suffers from similar artifacts.

For CMCT reconstruction, we propose a modified local CT algorithm, in which both global and local projection data are used. The local micro-CT projection data P_{local} involved with a VOI, Ω, are sampled in a fine grid, while the global medical CT projection data P_{global} are sampled in a coarse grid. If both P_{local} and P_{global} are acquired in the same scanning geometry, we can combine the 2 datasets as

$$P^{c}_{global} = \begin{cases} P_{local}, & if\ P_{local}\ is\ defined; \\ P^{i}_{global}, & otherwise, \end{cases} \tag{12}$$

where P^{i}_{global} denotes the linear interpolation of P_{global} on the fine grid of P_{local}. Let P^{t}_{global} be the true global projection data in the fine grid. Our modified local CT algorithm is based on the following observation

$$R_{\vec{x}}\left(P^{c}_{global} - P^{i}_{global}\right) \approx R_{\vec{x}}\left(P^{t}_{global} - P^{i}_{global}\right) \tag{13}$$

for each point $\vec{x}\in\Omega$, where $R_{\vec{x}}(P)$ denotes an appropriate reconstruction operator at point $\vec{x}$ from the projection data P. This property is consistent to our earlier wavelet multiresolution CT results (10,23,24).

The physical meaning of (13) is also clear. Since $P^{c}_{global} - P^{i}_{global}$ coincides with $P^{t}_{global} - P^{i}_{global}$ in the projection region of the VOI, and contains only information with frequencies higher than that contained in P_{global}, the reconstruction from $P^{c}_{global} - P^{i}_{global}$ via $R_{\vec{x}}$ for $\vec{x}\in\Omega$ is basically a local operation and a good approximation to $\vec{x}\in\Omega$, provided that the coarse grid is not too rough. Let us define the fine-to-coarse ratio (FCR) between the sampling frequencies of fine and coarse grids. The appropriate FCR depends on the size of the VOI. The smaller the size, the higher the ratio. Since the Radon transform is a linear operation, the reconstruction from P^{c}_{globle} can be written as

$$\begin{aligned} R_{\vec{x}}\left(P^{c}_{global}\right) &= R_{\vec{x}}\left(P^{c}_{global} - P^{i}_{global}\right) + R_{\vec{x}}\left(P^{i}_{global}\right) \\ &\approx R_{\vec{x}}\left(P^{t}_{global} - P^{i}_{global}\right) + R_{\vec{x}}\left(P^{i}_{global}\right) = R_{\vec{x}}\left(P^{t}_{global}\right) \end{aligned} \tag{14}$$

for each reconstruction point $\vec{x}\in\Omega$. Therefore, our algorithm should not be subject to any significant image cupping and intensity shifting artifacts.

CMCT Reconstruction

In CMCT, global and local projection data will be obtained in different scanning geometries, which are denoted by G_{local} and G_{global} respectively. For data registration, a facial surface model S_{local} is required as the reference framework. In practice, S_{local} can be constructed using the laser surface scanner. We propose the following algorithm for reconstruction of a VOI:

1. [**Registration**] Align P_{global} with P_{local} in reference to the local scanning geometry G_{local}.
   a. Reconstruct a global image I_{global} from P_{global};
   b. Render the surface S_{global} from the image I_{global};
   c. Align S_{global} with S_{local} using the linear conformal transformation under the assumption that the S_{global} and S_{local} are linked by some combination of translation, rotation, and scaling;
   d. Perform a forward projection of the aligned im-

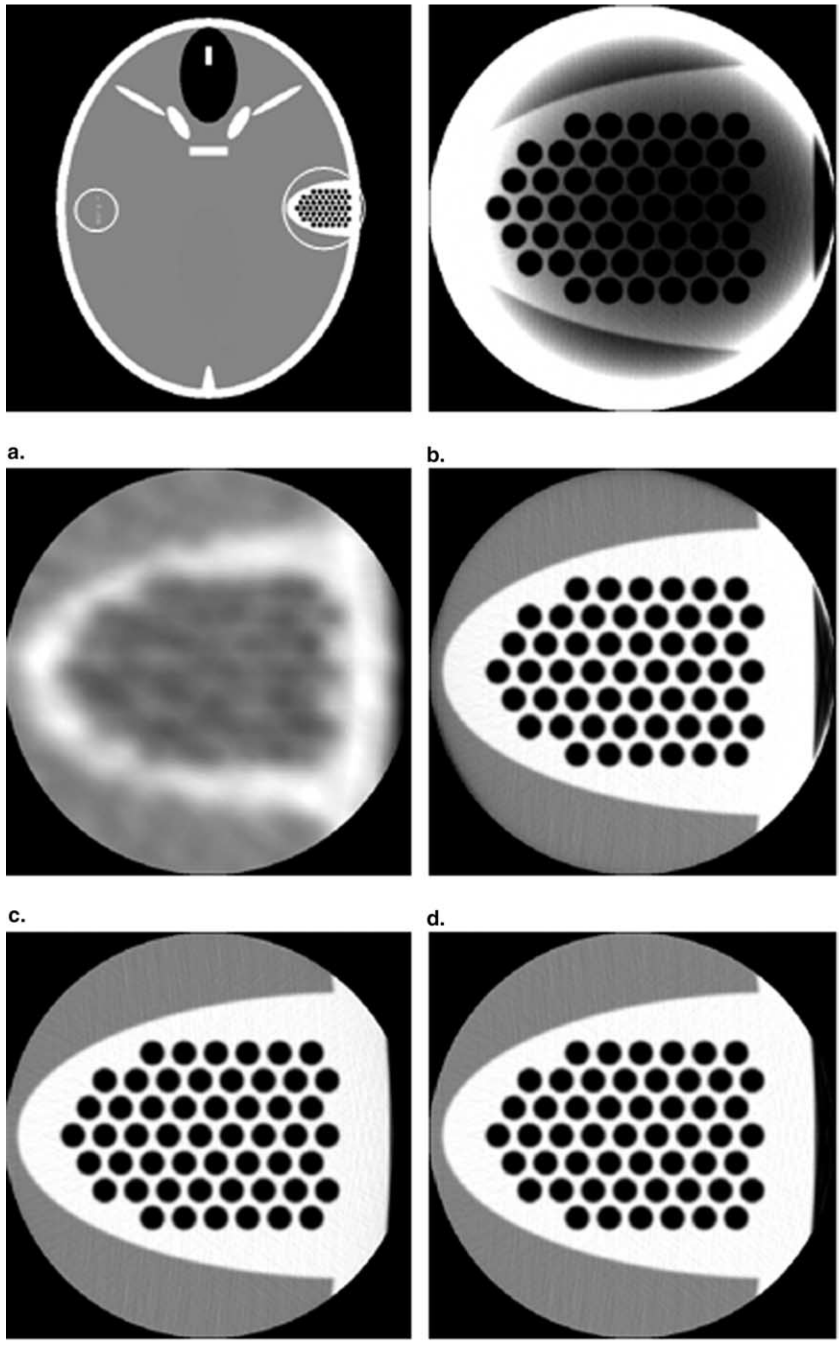

Figure 3. Local ROI reconstructions of the left inner ear. **(a)** The head phantom with two ROIs in white circles, **(b)** a pure local reconstruction showing cupping and shifting artifacts where the display window is shifted up by 1333 HU, **(c)** a global reconstruction with RCR = 8, **(d–f)** our modified local reconstructions with the FCR of 32, 16, and 8, respectively.

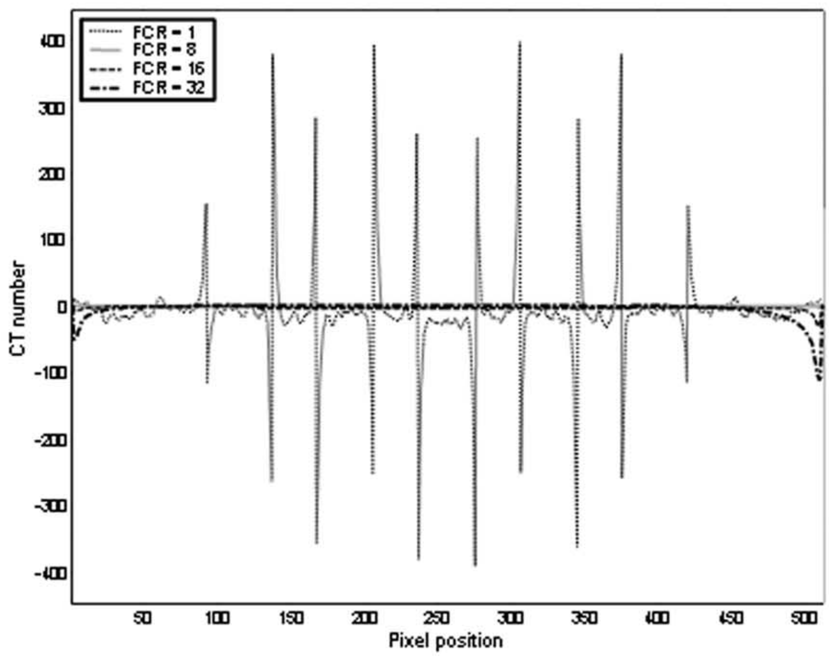

a.

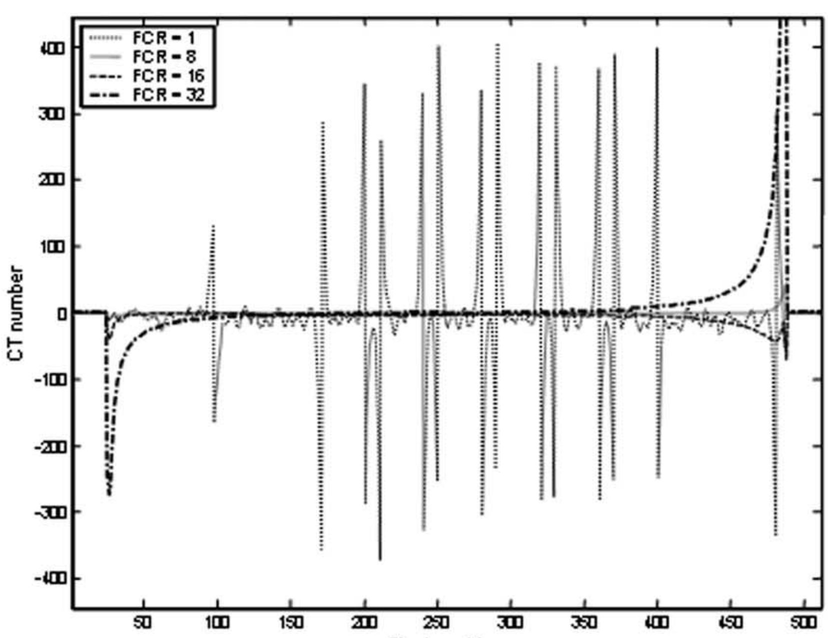

b.

Figure 4. Error plots through the representative lines in the images: **(a)** x = 266 and **(b)** y = 150. The curve for FCR = 1 stands for the error with the highest resolution global reconstruction, while other curves show the differences between various local CT images and the global reconstruction. When FCR $>$ 8 there is no significant difference between the truth and the reconstruction, as quantified by a noise standard deviation $<$ 5 HU.

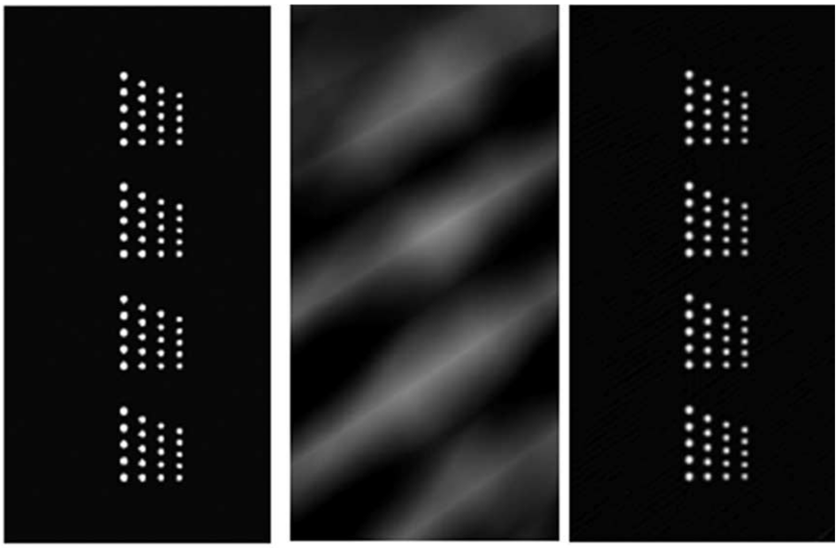

a. b. c.

Figure 5. Local ROI reconstructions of the right inner ear. **(a)** The phantom image of the ROI, **(b)** a low-resolution global reconstruction of the ROI, **(c)** a high resolution modified local CT reconstruction.

age I^{a}_{global} to obtain the corresponding global projection data P^{a}_{global} in a coarse grid with respect to G_{local}.

2. [**Interpolation**] Combine P^{a}_{global} with P_{local} in the local scanning geometry G_{local}.
   a. Interpolate P^{a}_{global} to a fine grid matching with P_{local};
   b. Complete P_{local}-missed portions by interpolating appropriate parts of P^{a}_{global}.
3. [**Reconstruction**] Reconstruct the VOI in the local scanning geometry G_{local} from the combined cone-beam projection data using a modified Feldkamp algorithm.

RESULTS

Preliminary tests were performed to demonstrate the feasibility of our modified local CT algorithm. The 2 local ROIs were selected from the head phantom [http://www.imp.uni-erlangen.de/forbild/deutsch/results/head/head.html], as shown in Figure 3(a). In the first test, a left-side ROI of radius 2.56 cm was used to generate projection data in a 672 × 1160 sampling grid. These data were reconstructed incorporating low-resolution global projections with FCR of 32, 16, and 8, respectively. Figure 3(b) shows a pure local reconstruction, where strong cupping and shifting artifacts are evident. Figure 3(c) shows a global reconstruction with FCR = 8. Figure 3(d–f) are the modified local reconstructions for 3 FCR values 32, 16, and 8, respectively. They are free of visible artifacts. Figure 4 indicates that the differences between modified local and high-resolution global reconstructions are insignificant if one considers the error range due to the filtered back-projection (FBP) procedure. In the second test, a right ROI of radius 1 cm was chosen. Low-resolution global and high-resolution local projections were generated on sampling grids of 84 × 145 and 2688 × 2320, respectively, with the FCR being 32 × 16. Figures 5–7 demonstrate that the image quality in the VOI reconstruction is excellent with a mean square error less than 0.0001 as compared to the standard high-resolution reconstruction.

The feasibility of the proposed CMCT system was also tested using real clinical CT (Siemens SOMATOM Sensation 16) and micro-CT (SkyScan 1076; SkyScan, Aartselaar, Belgium) scans of a cat skull whose cochlea was implanted with a feline model of a Cochlear Corporation electrode array. The cat skull was selected because of both its anatomical similarity to the human skull and the matching of its size to the current micro-CT imaging aperture. This skull presents detailed internal structures, and its dimensions are appropriate for both CT and micro-CT

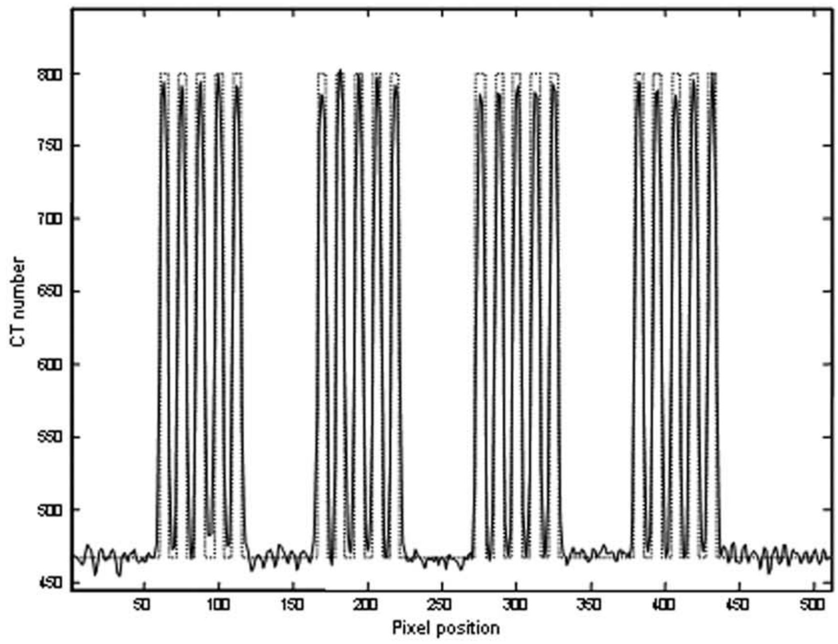

a.

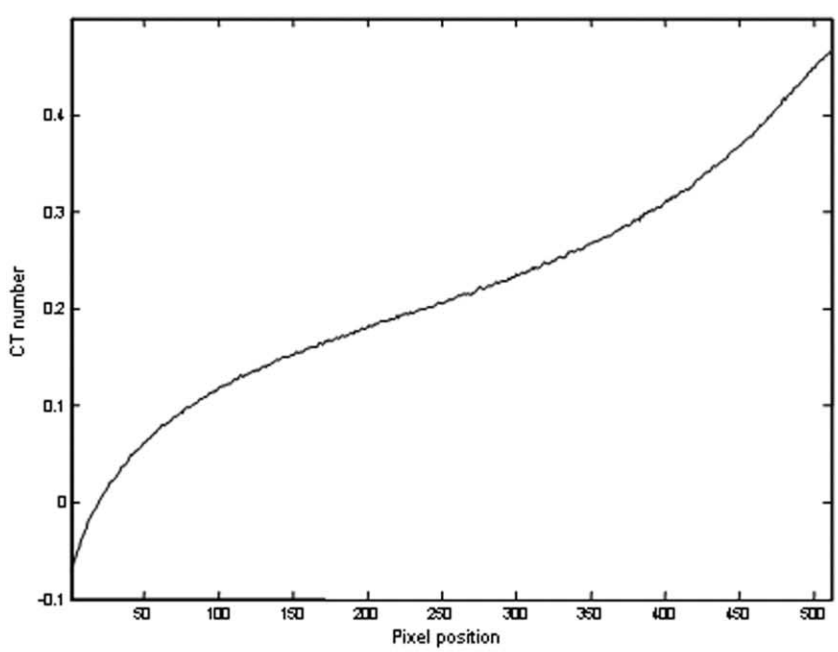

b.

Figure 6. Profiles along the line x = 150. **(a)** Profiles of the true phantom (thin dashed line) and modified local reconstruction data (thick solid line), **(b)** difference between modified local CT and global reconstructions.

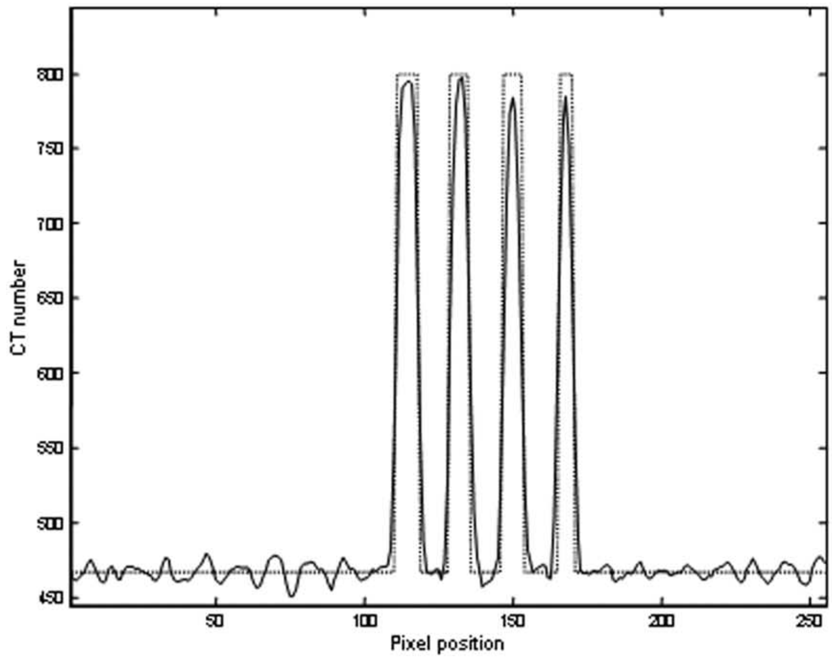

a.

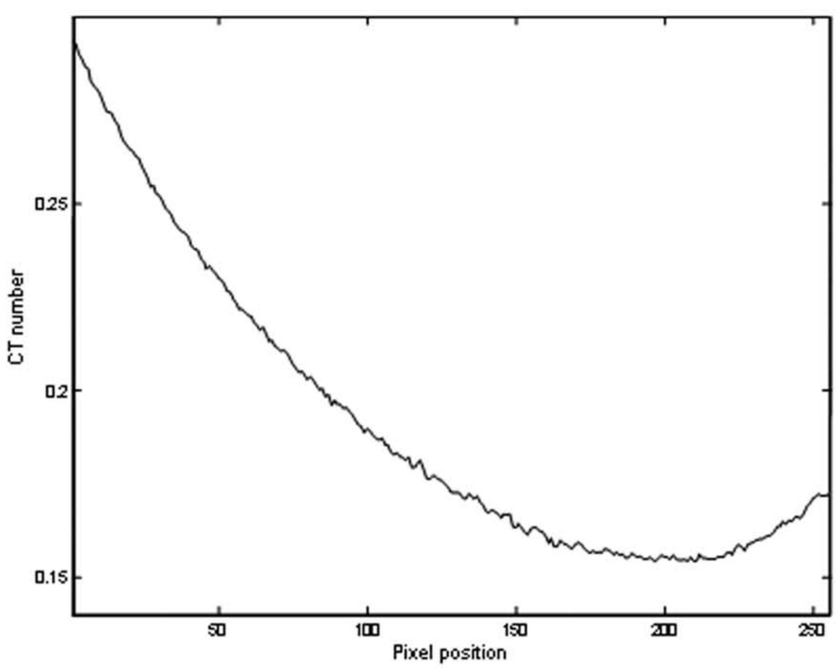

b.

Figure 7. Profiles along the line 4 = 170. **(a)** Profiles of the true phantom (regular) and modified local reconstruction data (irregular), **(b)** differences between modified local CT and global reconstructions.

Table 2
Screening Parameters of the Clinical CT and Micro-CT Scans of the Implanted Cat Skull

		Siemens SOMATOM Sensation 16	SkyScan 1076
X-ray tube voltage		120 kV	100 kV
X-ray tube current		250 mA	100 μA
Scanning locus		Helix (pitch = 12 mm)	Circle
Views per rotation		1160	800
Object-to-source distance		570 mm	121 mm
Detector	Field of view	500 mm	67 mm
	Columns	1344	1872
	Rows	16	524

scans to provide complete datasets and reveal rich information. Hence, we can easily mimic any local micro-CT scan and evaluate the effectiveness of the proposed CMCT approach. The CT and micro-CT scans were performed using a Siemens SOMATOM Sensation 16 scanner and a SkyScan 1076 micro-CT Scanner according to the protocols summarized in Table 2. Then, 2 cylindrical volumes of radius 34.0 mm and height 7.7 mm were reconstructed from low-resolution global and high-resolution local projections respectively in 1968 × 1968 × 211 matrices using our in-house software. As demonstrated in Figure 8(a,b), the image from CT projections is significantly more blurry than that from micro-CT projections since CT detectors are much larger than micro-CT detectors. In this cylindrical volume, we are particularly interested in the cochlea marked with a white circle (diameter 28.5 mm) in Figure 8. In the CMCT reconstruction, we used a one-fifth subsampled clinical-CT raw datum as the global dataset. The selected local micro-CT dataset was then merged with the global CT dataset with the FCR being 50. Finally, the VOI was reconstructed from the combined sinogram using our CMCT method described in the preceding section. The CMCT reconstruction of the implanted cat skull is presented in Figures 8(c) and (d). In the VOI, the difference between Figures 8(c) and (b) is very small with the mean square error 0.0036. These results show that the visibility of the implanted electrode array is excellent with individual electrodes being well depicted in their anatomical context.

DISCUSSION AND CONCLUSION

In one aspect, the CMCT system comprises a modified clinical CT scanner. A microimaging chain comprising a microfocused X-ray tube and a 1D or 2D high-resolution X-ray detector array can be added into the CT gantry to complement the traditional CT data acquisition system. Optionally, this microimaging capability can be embedded in the traditional CT data acquisition system, for example, using an X-ray tube with multiple focal spot sizes and a detector array with various binning modes. In this aspect, an optical surface scanner may not be used. A traditional CT scan of a patient's head (or other body region) can be performed when the head is kept stationary in an immobilization mechanism such as a head holder. Then a region/volume of interest in the head is outlined in a CT volume of the head. The head can be repositioned by steering the head (for example, via moving a patient table) so that the center of the region/volume of interest coincides with the isocenter of the CT gantry. The microimaging chain is accordingly aligned to focus with respect to this isocenter with an adjustable fan-beam/cone-beam aperture for subsequent micro-CT/micro-tomosynthesis scans. The head can also be kept stationary, while the microimaging can be done by adaptive collimation through the region/volume of interest toward a high-resolution detector array. The CT and micro-CT/microtomosynthesis datasets can be reconstructed into desirable images using the above described methods.

Recently, the interest in tomosynthesis has been renewed due to the development of digital detectors, reconstruction theory and methods, high performance PCs, as well as concern over radiation exposure. Various tomosynthesis techniques and systems have been developed and applied for breast cancer screening, pulmonary nodule detection, orthopaedics, angiography, dental imaging, and so on (25–32). We emphasize that the solution to this incomplete data/limited angle problem is an attractive option for our proposed CMCT system for the same reasons behind other tomosynthesis applications. Primarily, despite its inferior image quality relative to that of CT/micro-CT, tomosynthetic imaging may dramatically reduce the radiation dose because it requires only a small fraction of complete projection data (33).

We emphasize that systematic evaluation and optimization of the registration techniques are critically important for precise fusion of the medical CT and micro-CT data/images. In this regard, both hardware and software efforts are needed. Fortunately, both surface and image registration techniques have been actively developed for years. Therefore, we can utilize many proven methods and products for our purpose and make improvements when necessary. On the other

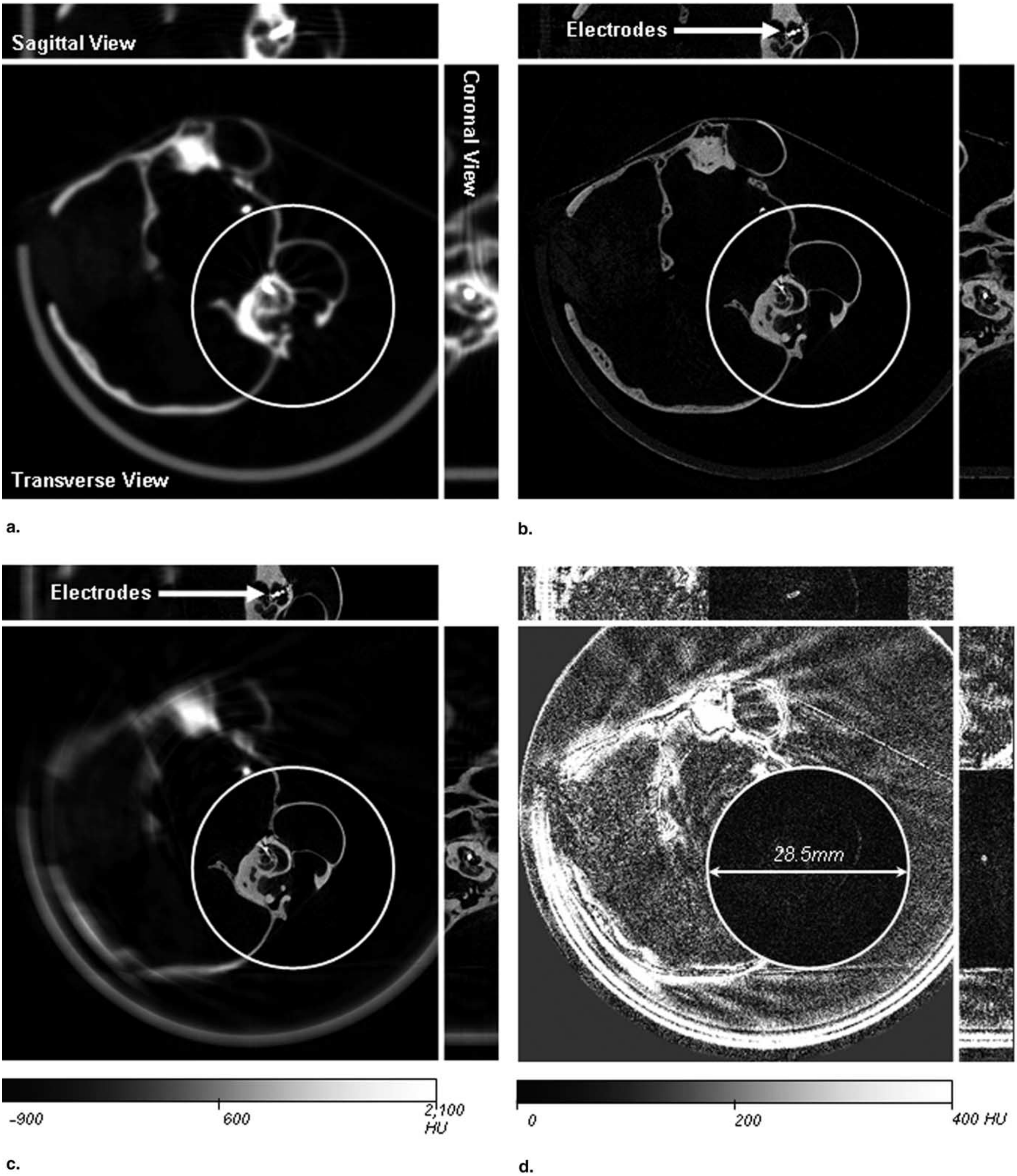

Figure 8. CMCT reconstruction of an implemented cat skull using our in-house software based on clinical CT and Micro-CT scans **(a)** Transverse, sagittal and coronal slices reconstructed from data acquired by a Siemens SOMATOM Sensation 16 scanner, **(b)** corresponding slices reconstructed from data acquired by a SkyScan 1076 micro-CT scanner **(c)** corresponding slices reconstructed using our CMCT approach; **(d)** the difference image between **(c)** and **(b)**.

hand, until now most of the work on registration has been done in the image domain. A direction we consider promising is to merge data, instead of images, from different tomographic imaging modalities. In our case, micro-CT data would be fused with medical CT data despite their differences in resolution and sampling geometry. We are studying relevant issues to fully utilize the CMCT potentials.

We recognize that the system characterization and optimization must be performed in large phantom experiments with appropriate X-ray tubes and detectors. In this regard, we will rely primarily on cadaver head experiments because they provide realistic simulations of the clinical imaging conditions. As far as X-ray sources are concerned, The X-ray Tubes-Vacuum Technology Division of the Siemens Medical Systems (http://www.med.siemens.com/med/rv/x_ray_tubes/) is one possible supplier. This company provides both microfocus sources and high-performance tubes; it also meets specialized needs for X-ray sources. Regarding X-ray detectors, we may use direct conversion flat panel detectors, which represent the state-of-the-art of the field. When our project enters the prototyping stage, we will have more experimental data to make an optimal selection of the critical components. Also, we remark that the X-ray energy optimization should be performed with respect to spectral width and mean photon energy based on the results obtained by Grodzins (34,35) and Spanne (36), which will be systematically addressed in further research.

As far as the number of beneficiary patients is concerned, it is well known that significant hearing impairment occurs in approximately 10% of the US population. The CMCT technology will be a general imaging tool for diagnosis and intervention in many inner ear diseases. Furthermore, the CMCT system has the potential to improve the safety of guiding cochlear implant electrodes within the inner ear and to assist the placement of inner ear microcatheters for delivery of gene modification therapy or administration of neurotrophic factors. Although immediate applications are for temporal bone imaging, extensions to other clinical applications are envisioned. Imaging of microarchitectures of the cancellous bone is an important example.

In conclusion, we have proposed the first clinical micro-CT (CMCT) system for human temporal bone imaging in vivo. The main feature of our approach is to integrate global medical CT data with local micro-CT/microtomosynthetic data for local microimaging at the minimum X-ray dose level. Our system design and simulation results demonstrate that the proposed system is feasible and holds great promise for inner ear and other clinical applications.

ACKNOWLEDGMENT

This work is partially supported by NIH grants DC03590, EB002667 and EB004287.

REFERENCES

1. DiBianca FA, Gupta V, ZHD. A variable resolution X-ray detector for computed tomography: I. Theoretical basis and experimental verification. Medical Physics 2000; 27:1865–1874.
2. DiBianca FA, et al. A variable resolution X-ray detector computed tomography: II. Imaging theory and performance. Medical Physics 2000; 27:1875–1880.
3. Wang G, Zhao S, inventors; University of Iowa Research Foundation, assignee. Clinical micro-CT (CMCT) methods, techniques and apparatus. US Provisional Patent Application, Filing Date: November 24, 2004.
4. Faridani A, et al, Local tomography II. SIAM J Appl Math 1997; 57: 1095–1127.
5. Faridani A, Ritman EL, Smith KT. Local tomography. SIAM J Appl Math 1992; 52:459–484.
6. Berenstein C, Walnut D. Local inversion of the Radon transform in even dimensions using wavelets. In: Gindikin S, Michor P, eds. 75 Years of Radon Transform. Cambridge, MA: International Press, 1994; 45–69.
7. Berenstein C, Walnut D. Wavelets and local tomography. In: Aldroubi A, Unser MA, eds. Wavelets in Medicine and Biology. Boca Raton, FL: CRC Press, 1996; 231–262.
8. Olson T, DeStefano J. Wavelet localization of the Radon transform. IEEE Trans Signal Proc 1994; 42:2055–2067.
9. Zhao S, Wang G. Wavelet operators and their applications in computerized tomography. In Mathematical Imaging 1997: International Symposium on Optical Science, Engineering, and Instrumentation. Proceedings of SPIE, San Diego, CA, July 27-August 1, 1997. Bellingham, WA: The International Society for Optical Engineering; 1997; 337–348.
10. Zhao S, Welland GV, Wang G. Wavelet sampling and localization schemes for the Radon transform in two dimensions. SIAM J Appl Math 1997; 57:1749–1762.
11. Folowpsels FO, Camp JJ, Brey RH, Lane JI, Robb RA. 3D Imaging and Modeling of the Middle and Inner Ear. in Proc. SPIE - Medical Imaging 2004, Visualization, Image-Guided Procedures, and Display, 5367:508–515, 2004.
12. Lane JI, et al. Imaging microscopy of the middle and inner ear: Part I: CT microscopy. Clin Anat 2004; 17:607–612.
13. Feldkamp LA , Davis LC, Kress JW. Practical cone-beam algorithm. J Opt Soc Am 1984; 1(A):612–619.
14. Noo F, et al. Image reconstruction from fan-beam projections on less than a short scan. Phys Med Biol 2002; 47:2525–2546.
15. Yu H, Wang G. Feldkamp-type VOI reconstruction from super-short-scan cone-beam data. Med Phys 2004; 31:1357–1362.
16. Barrett HH, Gordon SK, Hershel RS. Statistical limitations in transaxial tomography. Comput Biol Med 1976; 6:307–323.
17. Swindell W, et al. Computed tomography with a linear accelerator with radiotherapy applications. Med Phys 1983; 10:416–420.
18. Wagner RF, Brown DG, Pastel MS. Application of information theory to the assessment of computed tomography. Med Phys 1979; 2:83–94.
19. Chesler DA, Riederer SJ, Pelc NJ. Noise due to photon counting statistics in computed x-ray tomography. J Comput Assist Tomogr 1977; 1:64–74.
20. Wang G, et al. Spiral CT image deblurring for cochlear implantation. IEEE Trans Med Imaging 1998; 17:251–62.

21. Wang G, Schweiger G, Vannier MW. An iterative algorithm for X-ray CT fluoroscopy. IEEE Trans Med Imaging 1998; 17:853–856.
22. Natterer F. The Mathematics of Computerized Tomography. New York: John Wiley and Sons, 1986.
23. Zhao S. Wavelet filtering for filtered backprojection in computed tomography. Appl Comput Harmon Anal 1999; 6:346–373.
24. Zhao S, Wang G, Hsieh J. A wavelet filtering algorithm for fan-beam CT. IEE Electronics Letters 1998; 34:2395–2396.
25. Dobbins JT 3rd, Godfrey DJ. Digital x-ray tomosynthesis: current state of the art and clinical potential. Phys Med Biol 2003; 48:R65–106.
26. Sone S, et al. Development of a high-resolution digital tomosynthesis system and its clinical applications. Radiographics 1991; 11:807–822.
27. Sone S, Kasuga T, Sakai F. Digital Tomosynthesis Imaging of the Lung. Diagnostic Radiology 1996; 14:53–63.
28. Godfrey DJ, Rader A, Dobbins JT. III. Practical strategies for the clinical implementation of matrix inversion tomosynthesis (MITS). In Medical Imaging 2003: Physics of Medical Imaging. Proceedings of SPIE, San Diego, CA, February 15–20, 2003. Bellingham, WA: The International Society for Optical Engineering; 2004; 397–390.
29. Godfrey DJ, Dobbins JT. Optimization of matrix inversion tomosynthesis via impulse response simulations. Radiology 2002; 225:545–546.
30. Duryea J, Dobbins JT 3rd, Lynch JA. Digital tomosynthesis of hand joints for arthritis assessment. Med Phys 2003; 30:325–333.
31. Stevens GM, Fahrig R, Pelc NJ. Filtered backprojection for modifying the impulse response of circular tomosynthesis. Med Phys 2001; 28: 372–380.
32. Stevens GM, Fahrig R, Pelc NJ. Filtered-backprojection for improved blurring in circular tomosynthesis. Radiology 2000; 217:314–315.
33. Boone JM, et al. Dedicated breast CT: Radiation dose and image quality evaluation. Radiology 2001; 221:675–667.
34. Grodzins L. Optimum energies for x-ray transmission tomography of small samples: Applications of synchrotron radiation to computerized tomography I. Nuclear Instruments and Methods in Physics Research 1983; 206:542–545.
35. Grodzins L. Critical absorption tomography of small samples: proposed applications of synchrotron radiation to computerized tomography II. Nucl Instrum Methods Phys Res 1983; 206:547–552.
36. Spanne P. X-ray energy optimisation in computed microtomography. Phys Med Biol 1989; 34:679–690.